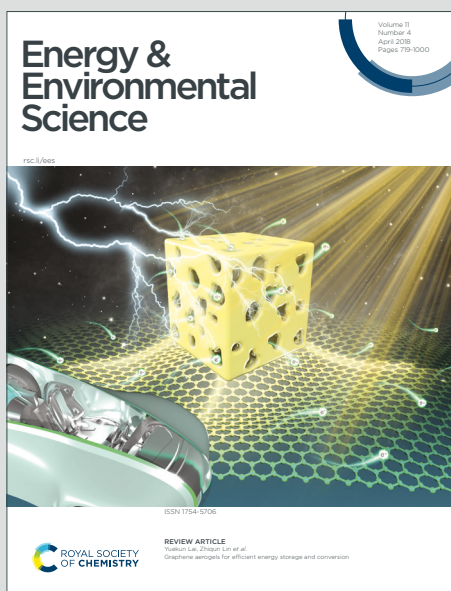


# Energy & Environmental Science

Accepted Manuscript

This article can be cited before page numbers have been issued, to do this please use: Y. Liu, X. Li, H. Jang, J. Wu, M. G. Kim, X. Xi, Z. Lei, Y. Zhang, Y. Deng, W. Yan, J. Jiang, S. Jiao, J. Luo and R. Cao, *Energy Environ. Sci.*, 2025, DOI: 10.1039/D4EE05220J.



This is an Accepted Manuscript, which has been through the Royal Society of Chemistry peer review process and has been accepted for publication.

Accepted Manuscripts are published online shortly after acceptance, before technical editing, formatting and proof reading. Using this free service, authors can make their results available to the community, in citable form, before we publish the edited article. We will replace this Accepted Manuscript with the edited and formatted Advance Article as soon as it is available.

You can find more information about Accepted Manuscripts in the [Information for Authors](#).

Please note that technical editing may introduce minor changes to the text and/or graphics, which may alter content. The journal's standard [Terms & Conditions](#) and the [Ethical guidelines](#) still apply. In no event shall the Royal Society of Chemistry be held responsible for any errors or omissions in this Accepted Manuscript or any consequences arising from the use of any information it contains.

	Engineering Cao, Ruiguo; University of Science and Technology of China, Hefei National Laboratory for Physical Science at the Microscale, Department of Materials Science and Engineering

SCHOLARONE™  
Manuscripts

Open Access Article. Published on 25 February 2025. Downloaded on 2/25/2025 10:54:03 PM.

This article is licensed under a Creative Commons Attribution-NonCommercial 3.0 Unported Licence.



## Broader context

Proton exchange membrane (PEM) water electrolysis is a promising technology for sustainable hydrogen production. However, its large-scale application is hindered by the high cost and extreme scarcity of iridium-based oxide anodes. Recently, ruthenium-based catalysts have emerged as a viable alternative to Ir-based catalysts due to their lower cost and superior activity for acidic oxygen evolution reaction (OER). A major challenge for Ru-based catalysts is their poor stability, primarily caused by the continuous leaching of active sites under harsh acidic and oxidative conditions. Here, we present a self-limiting surface leaching mechanism that significantly enhances the long-term stability of RuMn solid oxide ( $\text{RuMnO}_x$ ) catalysts by suppressing continuous leaching. Characterization reveals that Mn partially dissolves from  $\text{RuMnO}_x$  during the initial stages of acidic OER, leading to the formation of a corrosion-resistant, Mn-vacancy-rich surface reconstruction layer. This unique structure effectively inhibits further leaching of Ru and Mn, thereby self-limiting the continuous degradation of the catalysts. As a result, the Mn-vacancy-rich  $\text{RuMnO}_x$  catalyst exhibits remarkable durability, surpassing 2500 hours at  $10 \text{ mA cm}^{-2}$  in  $0.5 \text{ M H}_2\text{SO}_4$ , along with an ultra-low overpotential of  $\sim 166 \text{ mV}$  at  $10 \text{ mA cm}^{-2}$ . In situ characterization and theoretical simulation demonstrate that the Mn vacancies increase the demetallation energy of Ru species and facilitate the formation of H-stabilized  $^*\text{OO}$  intermediate, significantly improving both long-term stability and catalytic activity.



## ARTICLE

## Self-Limiting Surface Leaching Stabilizes Ru-Based Catalysts for Acidic Water Oxidation†

Yang Liu,<sup>‡ab</sup> Xiyu Li,<sup>‡cd</sup> Haeseong Jang,<sup>‡ef</sup> Jianghua Wu,<sup>‡gh</sup> Min Gyu Kim,<sup>f</sup> Xiaoke Xi,<sup>a</sup> Zhanwu Lei,<sup>\*a</sup> Yuchen Zhang,<sup>a</sup> Yu Deng,<sup>i</sup> Wensheng Yan,<sup>j</sup> Jun Jiang,<sup>k</sup> Shuhong Jiao,<sup>\*k</sup> Jing-Li Luo<sup>\*b</sup> and Ruiguo Cao<sup>\*a</sup>Received 00th January 20xx,  
Accepted 00th January 20xx

DOI: 10.1039/x0xx00000x

Ru-based catalysts are a promising alternative to Ir-based catalyst for the acidic oxygen evolution reaction (OER), but their poor long-term stability remains a significant challenge. Continuous leaching-induced loss of active sites and structural collapse are the primary causes of this instability, severely limiting the practical application of Ru-based catalysts in proton exchange membrane (PEM) electrolyzers. Here, we present a self-limiting surface leaching mechanism that effectively suppresses continuous leaching, thereby significantly prolonging the lifespan of Ru-based catalysts under acidic OER conditions. Specifically, the Ru-Mn solid solution oxide with a hollow shell structure undergoes surface Mn leaching during the initial OER process, resulting in the formation of a Mn-vacancy-rich stable reconstruction layer. This layer effectively inhibits further leaching of both Ru and Mn, thus self-limiting the further degradation of catalysts. As a result, the reconstructed catalyst exhibits an unprecedented durability up to 2500 h at 10 mA cm<sup>-2</sup> in 0.5 M H<sub>2</sub>SO<sub>4</sub>. This remarkable stability was also validated in PEM electrolyzers, highlighting its practical applicability. Operando synchrotron characterizations combined with theoretical calculations reveal that the formation of Mn vacancies increases the demetallation energy of Ru species, thereby suppressing the continuous leaching and enhancing the long-term stability. This work provides valuable insights for designing highly stable catalysts through a self-limiting leaching mechanism.

## Introduction

Electrocatalytic water splitting powered by renewable energy provides a sustainable pathway for producing green hydrogen<sup>1-3</sup>. Among various water electrolysis techniques, PEM water

electrolysis stands out for its advantages over alkaline water electrolysis, including higher hydrogen purity, faster charge and ion conductivity, and quicker response times<sup>4-6</sup>. However, a major challenge in PEM water electrolysis is the sluggish four-electron transfer kinetics of the anodic acidic OER, which requires the development of efficient catalysts<sup>7-9</sup>. Currently, Ir-based catalysts are considered as the only practical acidic OER catalysts in PEM electrolyzers due to their robust stability in withstanding the harsh acidic and strong oxidative conditions<sup>10-12</sup>. However, the extreme scarcity and expensive price of Ir resources have seriously impeded their large-scale application in practical PEM electrolyzers<sup>13-15</sup>. To address these issues, researchers have focused on developing alternative non-Ir-based catalysts to reduce the cost of acidic OER catalysts. Among these, Ru- and Mn-based catalysts have been studied extensively for their advantages in catalytic activity for acidic OER<sup>4, 16-18</sup>. Unfortunately, the long-term stability of most Ru- and Mn-based catalysts reported to date remains limited to within tens of hours under high current density conditions in PEM electrolyzers, far short of the requirements for industrial application<sup>19-23</sup>.

The overoxidation and subsequent leaching of metal active sites under harsh acidic OER conditions often lead to crystal structure collapse and catalytic activity loss, which are the primary reasons for the poor stability of acidic OER catalysts<sup>24-26</sup>. Ru- and Mn-based catalysts, especially when used as anodes in PEM electrolyzers at high current densities, are particularly susceptible to this degradation mechanism<sup>27-29</sup>. Pourbaix diagrams indicate that the thermodynamically stable forms of

<sup>a</sup> Hefei National Laboratory for Physical Science at the Microscale, Department of Materials Science and Engineering, University of Science and Technology of China, Hefei, 230026, China.

E-mail: zwlei@mail.ustc.edu.cn, rgcao@ustc.edu.cn

<sup>b</sup> Shenzhen Key Laboratory of Energy Electrocatalytic Materials, Guangdong Provincial Key Laboratory of New Energy Materials Service Safety, College of Materials Science and Engineering, Shenzhen University, Shenzhen 518055, Guangdong, China.

E-mail: jingli.luo@ualberta.ca

<sup>c</sup> School of Physical Sciences, Great Bay University, Dongguan 523000, China.

<sup>d</sup> Songshan Lake Materials Laboratory, Dongguan, Guangdong, 523808, China.

<sup>e</sup> Department of Advanced Materials Engineering, Chung-Ang University, Gyeonggi-do, 17546, Republic of Korea.

<sup>f</sup> Department of Intelligent Energy and Industry, Chung-Ang University, 84 Heukseok-ro, Dongjak-gu, Seoul 06974, Republic of Korea.

<sup>g</sup> Department of Chemistry, Guangdong Provincial Key Laboratory of Catalysis, Southern University of Science and Technology, Shenzhen 518055, China.

<sup>h</sup> Suzhou Institute of Nano-Tech and Nano-Bionics (SINANO), Chinese Academy of Sciences, Suzhou 215123, China.

<sup>i</sup> National Laboratory of Solid-State Microstructures, Jiangsu Key Laboratory of Artificial Functional Materials, College of Engineering and Applied Sciences and Collaborative Innovation Center of Advanced Microstructures, Nanjing University, Nanjing 210093, China.

<sup>j</sup> National Synchrotron Radiation Laboratory, University of Science and Technology of China, Hefei, 230029, China.

<sup>k</sup> Key Laboratory of Precision and Intelligent Chemistry, University of Science and Technology of China, Hefei, 230026, China

E-mail: jiaosh@ustc.edu.cn

† Electronic supplementary information (ESI) available: supplementary figures and tables. See DOI: 10.1039/x0xx00000x

‡ These authors contributed equally to this work.



Ru and Mn under PEM operating conditions are soluble ruthenate ( $\text{RuO}_4$ ) and manganate ( $\text{MnO}_4^-$ ) species, respectively<sup>30, 31</sup>. Under the operation window in acidic electrolyzers, Ru and Mn ions tend to continuously leach from the catalyst, causing a gradual decline in catalytic activity<sup>32, 33</sup>. Subsequently, the continuous leaching often leads to the uncontrollable surface atom rearrangement, forming a reconstructed surface layer on the catalyst<sup>34-36</sup>. However, this reconstruction layer typically contains a high density of defects that cannot endure strong acidic and oxidative environment, leading to its rapid collapse and a significant loss in performance during acidic OER<sup>37-39</sup>. Therefore, developing structurally stable reconstruction layers to prevent the continuous leaching of metal active sites is essential for achieving highly stable acidic OER catalysts, though significant challenges remain.

Herein, we introduce a self-limiting surface leaching mechanism to develop a corrosion-resistant surface reconstruction layer on a RuMn-based catalyst, which significantly enhances its long-term stability (Figure 1a). Detailed characterization revealed that Mn partially dissolves from the RuMn solid solution oxide ( $\text{RuMnO}_2$ ) during the initial stages of the acidic OER, resulting in the formation of a Mn-vacancy-rich reconstruction layer on the catalyst surface ( $\text{V}_{\text{Mn}}\text{-RuMnO}_{2-x}$ ). Operando synchrotron studies combined with theoretical calculations demonstrated that Mn vacancies stabilize Ru species by increasing the demetallation energy of  $\text{RuO}_4$ , effectively preventing continuous ion leaching and improving long-term catalyst stability. Additionally, the cationic vacancies facilitate the formation of H-stabilized \*OO

intermediate and optimizes the electronic structure of Ru, lowering the free energy barrier for O-O bond formation and boosting catalytic activity. As a result, the  $\text{V}_{\text{Mn}}\text{-RuMnO}_{2-x}$  catalyst achieves unprecedented stability up to 2500 h at 10  $\text{mA cm}^{-2}$  with an ultra-low overpotential of  $\sim 166$  mV at 10  $\text{mA cm}^{-2}$  in 0.5 M  $\text{H}_2\text{SO}_4$ . Moreover, a PEMWE device incorporating  $\text{V}_{\text{Mn}}\text{-RuMnO}_{2-x}$  as the anode catalyst operated stably for over 600 h at 200  $\text{mA cm}^{-2}$ , manifesting its practical application potential.

## Results and discussion

### Self-limiting surface leaching mechanism and electrocatalytic performance of catalysts

To construct a binary metal oxide with a uniform mixture of Ru and Mn, we developed a chelation precipitation method combined with a one-step oxidation process to synthesize a Ru-Mn solid solution oxide with a hollow shell structure ( $\text{Ru}_{0.5}\text{Mn}_{0.5}\text{O}_2$ ) (Figure S1). For comparison, we also synthesized pure Ru oxide ( $\text{Ru}_1\text{Mn}_0\text{O}_2$ ) and pure Mn oxide ( $\text{Ru}_0\text{Mn}_1\text{O}_2$ ) using a similar method. As illustrated in Figure 1a,  $\text{Ru}_{0.5}\text{Mn}_{0.5}\text{O}_2$  undergoes a self-limiting surface leaching process under acidic OER conditions. During the initial OER process, Mn atoms may leach from the  $\text{Ru}_{0.5}\text{Mn}_{0.5}\text{O}_2$  catalyst with a relatively perfect rutile structure in the form of  $\text{MnO}_4^-$ , leading to the formation of a Mn-vacancy-rich surface reconstruction layer ( $\text{V}_{\text{Mn}}\text{-Ru}_{0.5}\text{Mn}_{0.5}\text{O}_{2-x}$ ). These vacancies can effectively suppress further leaching of both Ru and Mn and inhibit continuous catalyst degradation, thereby enabling the long-term stability of  $\text{V}_{\text{Mn}}\text{-Ru}_{0.5}\text{Mn}_{0.5}\text{O}_{2-x}$  during acidic OER.

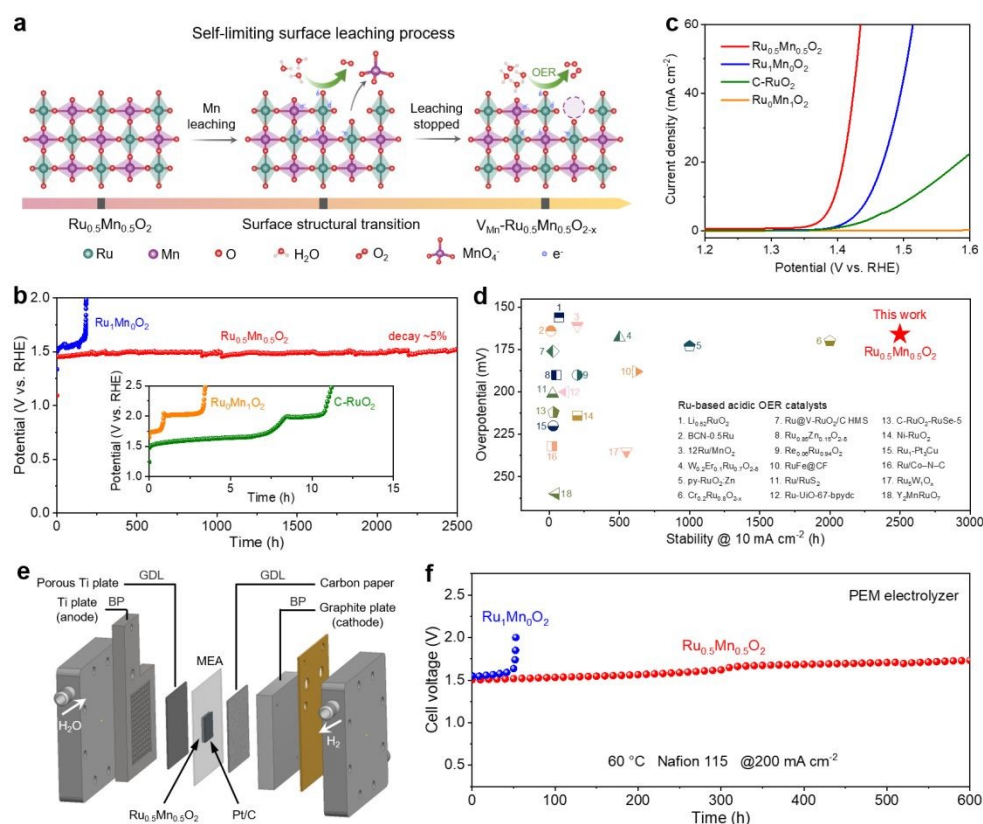


**Figure 1. Comparison of activity and stability of various catalysts.** (a) Schematic illustration of the self-limiting surface leaching process. (b) Chronopotentiometric curves of  $\text{Ru}_{0.5}\text{Mn}_{0.5}\text{O}_2$ ,  $\text{Ru}_1\text{Mn}_0\text{O}_2$ ,  $\text{Ru}_0\text{Mn}_1\text{O}_2$ , and C- $\text{RuO}_2$  at a current density of 10  $\text{mA cm}^{-2}$  in 0.5 M  $\text{H}_2\text{SO}_4$  solution.





(c) Polarization curves of  $\text{Ru}_{0.5}\text{Mn}_{0.5}\text{O}_2$ ,  $\text{Ru}_1\text{MnO}_2$ ,  $\text{Ru}_0\text{Mn}_1\text{O}_2$ , and C-RuO<sub>2</sub>. (d) Comparison of the overpotentials and stabilities for  $\text{Ru}_{0.5}\text{Mn}_{0.5}\text{O}_2$  and recently reported Ru-based OER catalysts in acid media. (e) Schematic diagram of the PEM electrolyzer. (f) Chronopotentiometry testing of PEM electrolyzers using  $\text{Ru}_{0.5}\text{Mn}_{0.5}\text{O}_2$  or  $\text{Ru}_1\text{MnO}_2$  as anodic catalyst and commercial Pt/C as cathodic catalyst operated at 200 mA cm<sup>-2</sup> at 60 °C.

We examined the long-term OER stability of  $\text{Ru}_{0.5}\text{Mn}_{0.5}\text{O}_2$  using chronopotentiometric measurements in 0.5 M H<sub>2</sub>SO<sub>4</sub>. Remarkably,  $\text{Ru}_{0.5}\text{Mn}_{0.5}\text{O}_2$  retained ~95% of its initial activity after 2500 hours at 10 mA cm<sup>-2</sup> (Figure 1b). Even at a higher current density of 100 mA cm<sup>-2</sup>, the potential increased by only 71 mV after 700 hours, highlighting the exceptional durability of  $\text{Ru}_{0.5}\text{Mn}_{0.5}\text{O}_2$  (Figure S2). In sharp contrast, C-RuO<sub>2</sub> and  $\text{Ru}_0\text{Mn}_1\text{O}_2$  only lasted a few hours of durability test at 10 mA cm<sup>-2</sup> (insert of Figure 1b). Although  $\text{Ru}_1\text{MnO}_2$  demonstrated improved long-term stability compared to C-RuO<sub>2</sub>, it still experienced severe activity loss after 180 h of durability test (Figure 1b). We also performed continuous cyclic voltammetry (CV) scanning tests to further evaluate the robustness of  $\text{Ru}_{0.5}\text{Mn}_{0.5}\text{O}_2$ . As shown in Figure S3, the overpotential of  $\text{Ru}_{0.5}\text{Mn}_{0.5}\text{O}_2$  at 10 mA cm<sup>-2</sup> increased by only 7 mV after 1 kth CV scans, significantly lower than the 40 mV increase observed for C-RuO<sub>2</sub>.

We evaluated the acidic OER performance of  $\text{Ru}_{0.5}\text{Mn}_{0.5}\text{O}_2$  using a three-electrode system with a 0.5 M H<sub>2</sub>SO<sub>4</sub> aqueous electrolyte. Linear sweep voltammetry (LSV) results indicate that  $\text{Ru}_{0.5}\text{Mn}_{0.5}\text{O}_2$  requires an overpotential of only ~166 mV to achieve a current density of 10 mA cm<sup>-2</sup>, outperforming  $\text{Ru}_1\text{MnO}_2$  (~218 mV) and C-RuO<sub>2</sub> (~285 mV) (Figure 1c). Notably,  $\text{Ru}_0\text{Mn}_1\text{O}_2$  shows negligible OER activity due to the absence of Ru active sites. To assess the intrinsic activity of  $\text{Ru}_{0.5}\text{Mn}_{0.5}\text{O}_2$ , we calculated the electrochemical specific surface area (ECSA) derived from the electrochemical double-layer capacitance ( $C_{dl}$ ) (Figure S4).  $\text{Ru}_{0.5}\text{Mn}_{0.5}\text{O}_2$  exhibited a larger ECSA than the other catalysts (Figure S5a), indicating more available active sites for OER. When normalizing the catalytic currents with respect to ECSA,  $\text{Ru}_{0.5}\text{Mn}_{0.5}\text{O}_2$  still exhibited the lowest overpotential among these catalysts (Figure S5b), confirming its superior intrinsic activity. In comparison,  $\text{Ru}_1\text{MnO}_2$  showed a similar overpotential to C-RuO<sub>2</sub> based on the ECSA analysis (Figure S5b), indicating that the Ru active sites in both catalysts possess comparable intrinsic activity. Furthermore,  $\text{Ru}_{0.5}\text{Mn}_{0.5}\text{O}_2$  achieves a high mass activity of 524.6 A g<sub>Ru</sub><sup>-1</sup> (normalized to Ru) at 1.45 V vs. RHE, which is approximately 11.1 times and 38.9 times higher than that of  $\text{Ru}_1\text{MnO}_2$  (47.2 A g<sub>Ru</sub><sup>-1</sup>) and C-RuO<sub>2</sub> (13.5 A g<sub>Ru</sub><sup>-1</sup>), respectively. These results unambiguously suggest  $\text{Ru}_{0.5}\text{Mn}_{0.5}\text{O}_2$  as one of the most active catalysts towards acidic OER, surpassing many Ru- or Ir-based catalysts reported in the literature (Figure S6). The Tafel slope for  $\text{Ru}_{0.5}\text{Mn}_{0.5}\text{O}_2$  was 41.8 mV dec<sup>-1</sup>, lower than  $\text{Ru}_1\text{MnO}_2$  (60.3 mV dec<sup>-1</sup>) and C-RuO<sub>2</sub> (94.3 mV dec<sup>-1</sup>), indicating its better OER kinetics (Figure S7). Electrochemical impedance spectroscopy (EIS) further supported these findings, revealing that  $\text{Ru}_{0.5}\text{Mn}_{0.5}\text{O}_2$  has the lowest charge transfer resistance (Figure S8 and Table S1), which implies faster charge transfer rate and OER kinetics. In addition, we investigated how the elemental composition of the solid-solution oxides influences their catalytic activity. By

adjusting the ratio of Ru and Mn chlorides, we synthesized a series of  $\text{Ru}_y\text{Mn}_{1-y}\text{O}_2$  catalysts ( $y = 0.9, 0.7, 0.3,$  and  $0.1$ ). Inductively coupled plasma atomic emission spectrometry (ICP-AES) analysis revealed that the Ru/Mn atomic ratios in  $\text{Ru}_y\text{Mn}_{1-y}\text{O}_2$  were close to the initial feed ratios (Figure S9 and Table S2). As shown in Figure S10,  $\text{Ru}_{0.5}\text{Mn}_{0.5}\text{O}_2$  demonstrated the highest OER activity among the tested catalysts, suggesting that a 1:1 ratio of Ru to Mn represents the optimal composition. A comparison of the activity and stability of  $\text{Ru}_{0.5}\text{Mn}_{0.5}\text{O}_2$  with recent reports in the literature revealed that it outperforms most Ru-based OER catalysts in acidic media (Figure 1d and Table S3)<sup>2, 36, 39-56</sup>.

Considering the high activity and stability of  $\text{Ru}_{0.5}\text{Mn}_{0.5}\text{O}_2$  for acidic OER, we assembled a PEM electrolyzer using the catalyst as the anode to evaluate its practical application potential. As shown in Figure 1e and Figure S11, the PEM electrolyzer was mainly composed of bipolar plates (BP), gas diffusion layers (GDL), and membrane electrode assembly (MEA). Among them, MEA with an active area of 4 cm<sup>2</sup> was manufactured by sandwiching a proton exchange membrane (Nafion 115) between the anode ( $\text{Ru}_{0.5}\text{Mn}_{0.5}\text{O}_2$ ) and cathode (commercial Pt/C). When the electrolyzer using  $\text{Ru}_{0.5}\text{Mn}_{0.5}\text{O}_2$  as the anode was operated at 60 °C, the steady-state polarization curve showed a cell voltage of 1.762 V to achieve a current density of 1 A cm<sup>-2</sup> (Figure S12), outperforming the electrolyzer using the  $\text{Ru}_1\text{MnO}_2$  as the anode (1.947 V@1 A cm<sup>-2</sup>). We further evaluated the durability of  $\text{Ru}_{0.5}\text{Mn}_{0.5}\text{O}_2$  in PEM electrolyzers. Impressively, the PEM electrolyzer with  $\text{Ru}_{0.5}\text{Mn}_{0.5}\text{O}_2$  as the anode operated at 200 mA cm<sup>-2</sup> for over 600 h without significant performance degradation (Figure 1f). In sharp contrast, PEM electrolyzer using  $\text{Ru}_1\text{MnO}_2$  as the anode exhibited severe decay after just 52 h of durability test at the same current density (Figure 1f). Furthermore, we increased the operating temperature and current density of the PEM electrolyzer to evaluate the long-term stability of the catalyst under more practical conditions. As shown in Figure S13, the PEM electrolyzer with  $\text{Ru}_{0.5}\text{Mn}_{0.5}\text{O}_2$  as the anode demonstrated stable operation for 330 h under 200 mA cm<sup>-2</sup> at 80 °C, and approximately 120 h under 500 mA cm<sup>-2</sup> at 60 °C. The elevated temperature and higher current density both adversely impacted the long-term stability of  $\text{Ru}_{0.5}\text{Mn}_{0.5}\text{O}_2$ , attributed to the harsher operating conditions encountered by the catalyst. These findings demonstrate the excellent activity and stability of  $\text{Ru}_{0.5}\text{Mn}_{0.5}\text{O}_2$  for acidic OER in PEM electrolyzers.

#### Self-limiting surface structural evolution of catalysts during acidic OER

We comprehensively characterized the morphology and structure of the catalysts before and after OER process to elucidate the structural evolution of  $\text{Ru}_{0.5}\text{Mn}_{0.5}\text{O}_2$ . First, we carried out scanning electron microscopy (SEM) and X-ray



diffraction (XRD) to investigate potential changes in morphology and crystalline structure of the catalysts. SEM images reveal that the prepared  $\text{Ru}_{0.5}\text{Mn}_{0.5}\text{O}_2$  catalysts displayed a hollow branch-like structure with abundant accessible channels (Figure S14a), which is beneficial for enhancing the electrochemical performance by boosting mass transfer of the reactant and product. Notably, the catalyst maintained its original hollow branch-like structure even after 50 h OER test (Figure S14b-d), as confirmed by low-magnification TEM images (Figure S15). The XRD patterns of the prepared  $\text{Ru}_{0.5}\text{Mn}_{0.5}\text{O}_2$  matched the rutile phase solid solution

of  $\text{RuO}_2$  and  $\text{MnO}_2$  ( $\text{P4}_2/\text{mnm}$  space group), confirming the formation of a solid-solution structure (Figure S16). Notably, the diffraction peaks of  $\text{Ru}_{0.5}\text{Mn}_{0.5}\text{O}_2$  shifts to higher angle compared to  $\text{Ru}_1\text{Mn}_0\text{O}_2$ , due to the substitution of Ru by Mn with a smaller ionic radius, leading to a reduction in interplanar spacing and an increase in the diffraction angle ( $\theta$ ), as described by the Bragg equation. After the OER testing, no significant changes were observed in the XRD patterns, indicating that post-OER  $\text{Ru}_{0.5}\text{Mn}_{0.5}\text{O}_2$  preserved its initial solid-solution phase (Figure S17).

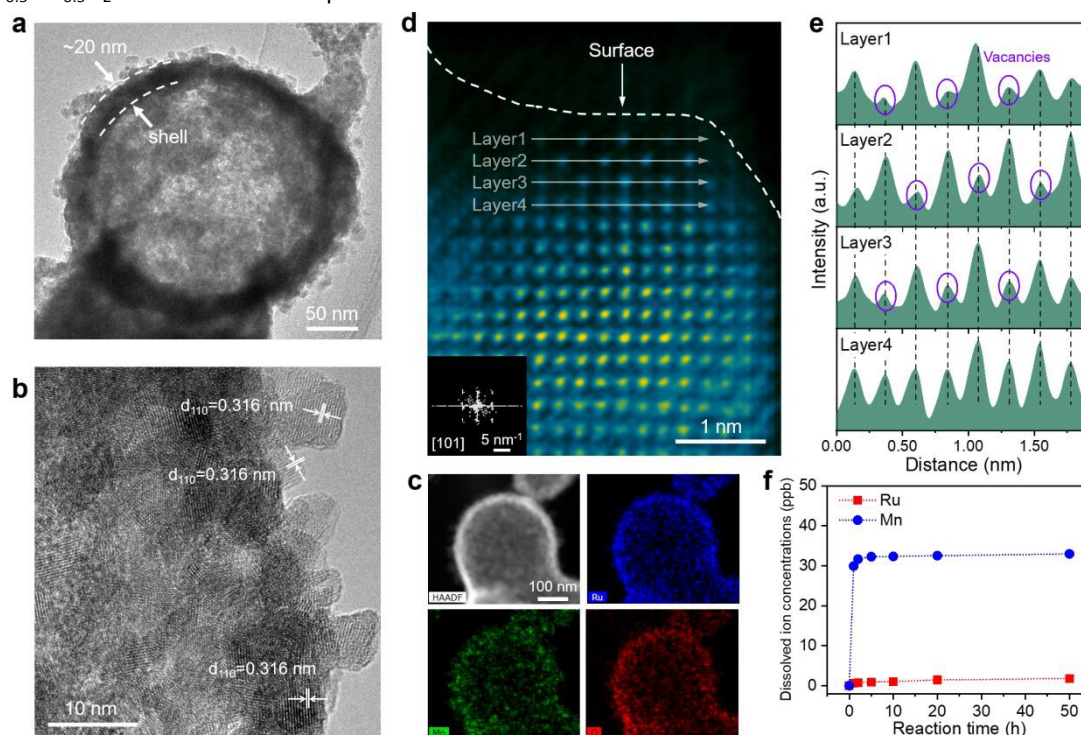


**Figure 2. Structural evolution of  $\text{Ru}_{0.5}\text{Mn}_{0.5}\text{O}_2$  during acidic OER process.** (a) Low-magnification TEM image of  $\text{Ru}_{0.5}\text{Mn}_{0.5}\text{O}_2$  after 50 h OER test. (b) HRTEM image of  $\text{Ru}_{0.5}\text{Mn}_{0.5}\text{O}_2$  after 50 h OER test. (c) HAADF image of  $\text{Ru}_{0.5}\text{Mn}_{0.5}\text{O}_2$  after 50 h OER test and the corresponding EDS elemental mappings of Ru, Mn, and O. (d) Atomic-resolution HAADF-STEM image of  $\text{Ru}_{0.5}\text{Mn}_{0.5}\text{O}_2$  after 50 h OER test from the [101] zone axis (inset: corresponding FFT pattern). (e) Corresponding intensity profiles over the selected atomic columns (layer1 to layer4 in (d)). (f) Dissolved Ru and Mn ion concentrations measured for  $\text{Ru}_{0.5}\text{Mn}_{0.5}\text{O}_2$  in electrolyte for different reaction times.

Subsequently, we utilized high-resolution TEM (HRTEM) to investigate the evolution of the surface structure on the catalyst during the acidic OER process. HRTEM images of the prepared  $\text{Ru}_{0.5}\text{Mn}_{0.5}\text{O}_2$  display clear lattice fringes with lattice spacings of 0.325 nm and 0.259 nm, corresponding to the (110) and (101) planes of rutile  $\text{RuO}_2$  (JCPDS: 43-1027), respectively (Figure S18a). The selected area electron diffraction (SAED) pattern, with distinct diffraction rings, confirmed its polycrystalline nature (Figure S18b). The average grain size is approximately 4.7 nm (Figure S19). Energy-dispersive X-ray spectroscopy (EDX) mapping demonstrated a homogenous distribution of Ru, Mn, and O elements, further confirming the successful formation of RuMn solid-solution oxides (Figure S20). As a comparison, we also characterized the surface crystal structure of post-OER  $\text{Ru}_{0.5}\text{Mn}_{0.5}\text{O}_2$  using HRTEM. As shown in Figure 2a, b, the surface crystal structure of the post-OER  $\text{Ru}_{0.5}\text{Mn}_{0.5}\text{O}_2$  was well-

preserved, with interplanar spacings of 0.316 corresponding to the (110) planes of rutile  $\text{RuO}_2$ . Additionally, no noticeable amorphous reconstruction layers were observed on the catalyst surface. Elemental mapping (Figure 2c) and EDX line-scan analysis (Figure S21) of the post-OER  $\text{Ru}_{0.5}\text{Mn}_{0.5}\text{O}_2$  showed a uniform distribution of Ru, Mn, and O without significant segregation. These results collectively demonstrate that  $\text{Ru}_{0.5}\text{Mn}_{0.5}\text{O}_2$  catalyst retains both its morphology and crystalline structure during long-term acidic OER testing, highlighting its stability.

To further probe the atomic structure evolution of catalysts during acidic OER process, we employed aberration-corrected high-angle annular dark-field scanning transmission electron microscope (HAADF-STEM) on both the prepared and post-OER  $\text{Ru}_{0.5}\text{Mn}_{0.5}\text{O}_2$ . HAADF-STEM images of the prepared  $\text{Ru}_{0.5}\text{Mn}_{0.5}\text{O}_2$  showed well-crystallized nanocrystals without



significant defects (**Figure S22**). The corresponding Fast Fourier transform (FFT) pattern confirmed that the crystal structure aligns with the tetragonal crystal system of rutile  $\text{RuO}_2$  in the [111] projection (inset of **Figure S22a**). In contrast, the cation vacancies marked by purple circles is found in the post-OER  $\text{Ru}_{0.5}\text{Mn}_{0.5}\text{O}_2$  due to their lower intensity in the HAADF-STEM images (**Figure 2d, e**)<sup>57</sup>. Despite the presence of these vacancies, the surface atoms remained orderly arranged, and the crystal structure continued aligns with the tetragonal crystal system of rutile  $\text{RuO}_2$  in the [101] projection (inset of **Figure 2d**). Notably, these cation vacancies were predominantly located on the surface of the nanoparticles (**Figure 2d**), suggesting their formation is closely linked to irreversible ion dissolution occurring during the acidic OER process. This detailed analysis highlights the formation of surface cation vacancies as a key feature in the structural evolution of the catalyst during OER, which may play a significant role in influencing its performance and stability.

Additionally, we assessed the concentrations of Ru and Mn ions leached into the electrolyte during the acidic OER process from  $\text{Ru}_{0.5}\text{Mn}_{0.5}\text{O}_2$  using inductively coupled plasma-mass spectrometry (ICP-MS). As shown in **Figure 2f**, the dissolved Ru ion concentration consistently below 2 ppm throughout the 50 h OER test. In contrast, the dissolved Mn ion concentration rapidly increased to 31.69 ppb within the first 2 h and reached 32.33 ppb after 10 h, then plateaued. This uneven metal ion dissolution was further corroborated by EDS (**Figure S23** and **Table S4**) and X-ray photoelectron spectroscopy (XPS) (**Figure S24** and **Table S5**) analysis. Specifically, the atomic ratio of  $\text{Ru}/(\text{Ru}+\text{Mn})$  increased rapidly during the first 10 hours and then stabilized (**Figure S23e** and **Figure S24b**), reflecting the more pronounced leaching of Mn ions in the early stages of the OER process. Given that the leaching amount of Mn from the  $\text{Ru}_{0.5}\text{Mn}_{0.5}\text{O}_2$  is much greater than that of Ru, the cation vacancies observed in the post-OER  $\text{Ru}_{0.5}\text{Mn}_{0.5}\text{O}_2$  is mainly caused by the leaching of Mn ions. To further confirm the presence of Mn vacancies on the post-OER  $\text{Ru}_{0.5}\text{Mn}_{0.5}\text{O}_2$ , we employed electron paramagnetic resonance (EPR) spectroscopy. As shown in **Figure S25**, the post-OER  $\text{Ru}_{0.5}\text{Mn}_{0.5}\text{O}_2$  exhibits a stronger EPR peak at a g value of 2.003, which is attributed to unpaired electrons associated with Mn vacancies, compared to the pristine  $\text{Ru}_{0.5}\text{Mn}_{0.5}\text{O}_2$ . These Mn vacancies likely alter the local electronic structure surrounding the Ru active sites, thereby modulating the catalytic activity and stability of  $\text{Ru}_{0.5}\text{Mn}_{0.5}\text{O}_2$  with surface Mn vacancies ( $\text{V}_{\text{Mn}}\text{-Ru}_{0.5}\text{Mn}_{0.5}\text{O}_{2-x}$ ).

### Understanding the self-limiting surface leaching mechanism

To investigate the effect of cation vacancies on the electronic structure of catalytic active sites, we performed XAFS measurements to analyse the valence state and coordination environment of the active sites. As shown in **Figure 3a** and **Figure S26**, the valence state of Ru in  $\text{Ru}_{0.5}\text{Mn}_{0.5}\text{O}_2$  remained stable and below +4 during 50 h OER test, which was also demonstrated by Ru M-edge soft XAS (**Figure S27**), preventing the overoxidation and subsequent dissolution of high-valence

Ru species. In contrast, the valence state of Mn increased during the 50 h OER test according to Mn K-edge XANES spectra (**Figure S28**) and Mn L-edge soft XAS (**Figure S29**). To investigate the reasons behind the valence state changes of Ru and Mn during surface reconstruction, we first investigated the impact of Mn doping on the Ru valence state in  $\text{Ru}_{0.5}\text{Mn}_{0.5}\text{O}_2$ . As shown in **Figure S30**, Ru K-edge XANES spectra combined with absorption energy ( $E_0$ ) analysis reveal that the average Ru valence state in  $\text{Ru}_{0.5}\text{Mn}_{0.5}\text{O}_2$  (+3.60) is higher than that in  $\text{Ru}_1\text{Mn}_0\text{O}_2$  (+3.42), suggesting electron transfer from Ru to Mn via bridging oxygen atoms in  $\text{Ru}_{0.5}\text{Mn}_{0.5}\text{O}_2$ . This electron transfer is further supported by XPS and soft XAS data (**Figure S31**), where the peak positions for Ru in  $\text{Ru}_{0.5}\text{Mn}_{0.5}\text{O}_2$  shift to higher energies compared to those in  $\text{Ru}_1\text{Mn}_0\text{O}_2$ . Next, we analyzed the effect of Mn dissolution on the valence states of Ru and Mn. When Mn dissolves and forms cation vacancies in the catalyst, the oxidation states of both Ru and Mn in  $\text{V}_{\text{Mn}}\text{-Ru}_{0.5}\text{Mn}_{0.5}\text{O}_{2-x}$  would be expected to increase to maintain charge neutrality. However, experimental results show that only the oxidation state of Mn increases after Mn dissolution (**Figure S28**), while the oxidation state of Ru remains nearly unchanged (**Figure 3a**). This is because, after Mn dissolution and the formation of cation vacancies in  $\text{V}_{\text{Mn}}\text{-Ru}_{0.5}\text{Mn}_{0.5}\text{O}_{2-x}$ , the Ru atoms surrounding the cation vacancies no longer transfers electrons to the Mn atoms that have been replaced by vacancies. Consequently, the electron density of Ru increases, leading to a reduction in its oxidation state. In summary, the increase in oxidation state of Ru induced by charge neutrality and the decrease in its oxidation state due to weakened electron transfer ultimately stabilize the average oxidation state of Ru during the surface reconstruction process (**Figure 3a**).

We further examined the coordination environment changes of Ru and Mn by fitting the EXAFS spectra of  $\text{Ru}_{0.5}\text{Mn}_{0.5}\text{O}_2$  over different reaction times. As shown in **Figure 3b**, the Ru K-edge FT-EXAFS profiles of the  $\text{Ru}_{0.5}\text{Mn}_{0.5}\text{O}_2$  exhibited a prominent peak at 1.47 Å, corresponding to the first Ru-O coordination shell, and another peak at 2.97 Å, associated with Ru-Ru/Ru-Mn coordination in the second shell. EXAFS fitting analysis for the first-shell coordination revealed that both the bond length and coordination number (CN) of Ru-O bond remained largely unchanged throughout the 50 h OER process (**Figures S32** and **S33**, and **Table S6**). Notably, the second-shell EXAFS fitting results showed a decrease in the coordination number of Ru-Ru/Ru-Mn with increasing reaction time (**Figure 3c**), which can be attributed to the gradual rise in Mn vacancy concentration in the  $\text{V}_{\text{Mn}}\text{-Ru}_{0.5}\text{Mn}_{0.5}\text{O}_{2-x}$ . We also analysed the change of Mn coordination environment during OER process according to the Mn K-edge EXAFS spectra (**Figures S34** and **S35**, and **Table S7**). Similarly, the bond length and coordination number of Mn-O remain stable during the OER (**Figure S36**). Moreover, the coordination number of Mn-Ru/Mn-Mn generally show a decreasing trend with increasing reaction time, as revealed by the second-shell Mn K-edge EXAFS fitting (**Figure S37** and **Table S7**), further confirming the formation of Mn vacancies in the  $\text{Ru}_{0.5}\text{Mn}_{0.5}\text{O}_2$  catalyst during the OER process. These results confirm that the crystal structure framework of the solid solution remains intact throughout the





acidic OER process, accompanied by the formation of surface cation vacancies.

View Article Online

DOI: 10.1039/D4EE05220J

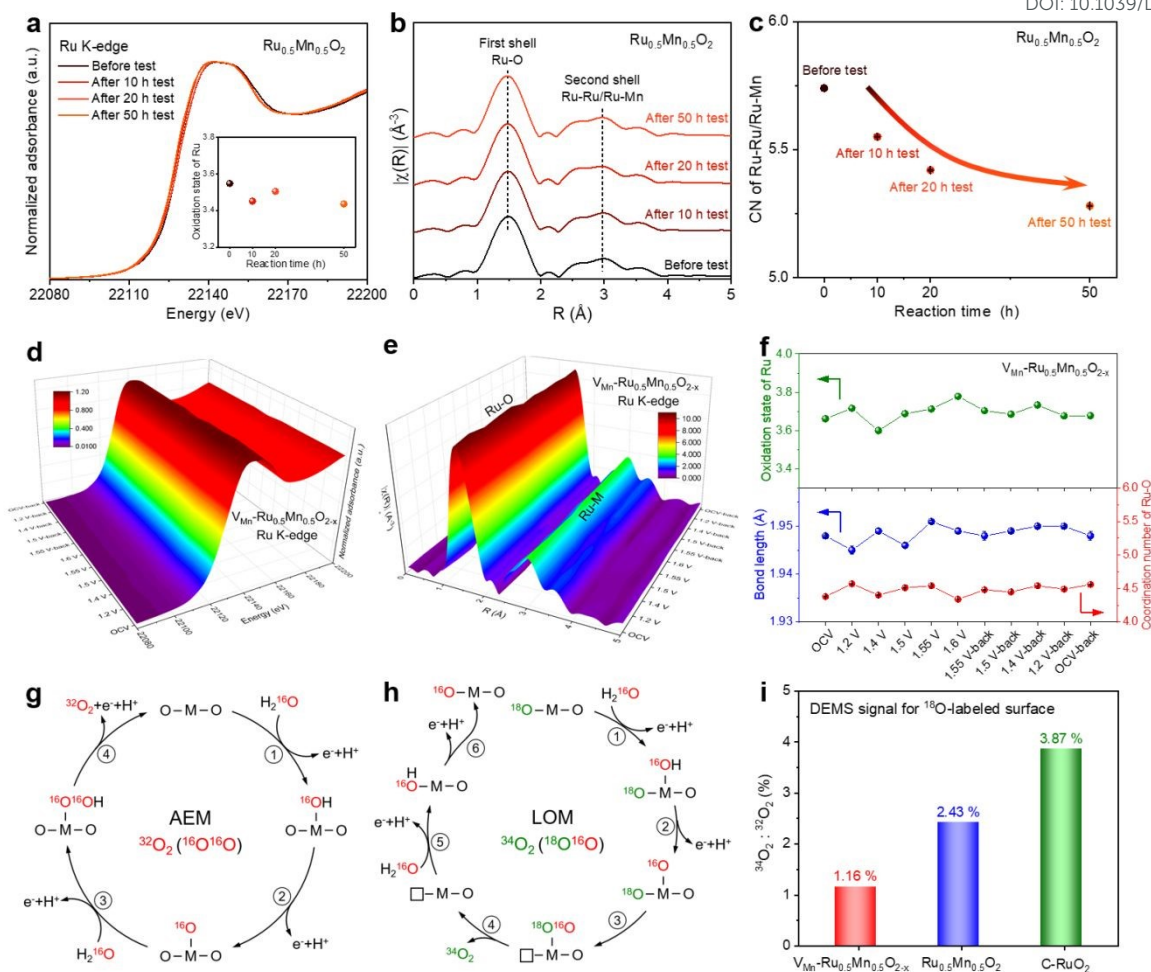


**Figure 3. Operando XAFS measurements and mechanism investigation.** (a) Ru K-edge XANES spectra of  $\text{Ru}_{0.5}\text{Mn}_{0.5}\text{O}_2$  before and after 10 h, 20 h, 50 h OER test (inset: the oxidation state of Ru under different reaction time). (b) Fourier-transformed Ru K-edge EXAFS spectra of  $\text{Ru}_{0.5}\text{Mn}_{0.5}\text{O}_2$  before and after 10 h, 20 h, 50 h OER test. (c) The coordination number of Ru-Ru/Ru-Mn for  $\text{Ru}_{0.5}\text{Mn}_{0.5}\text{O}_2$  before and after 10 h, 20 h, 50 h OER test. (d) 3D plot of operando Ru K-edge XANES spectra for  $\text{V}_{\text{Mn}}\text{-Ru}_{0.5}\text{Mn}_{0.5}\text{O}_{2-x}$ . (e) 3D plot of operando Ru K-edge EXAFS spectra for  $\text{V}_{\text{Mn}}\text{-Ru}_{0.5}\text{Mn}_{0.5}\text{O}_{2-x}$ . (f) The top image: The oxidation state of Ru under different applied potentials for  $\text{V}_{\text{Mn}}\text{-Ru}_{0.5}\text{Mn}_{0.5}\text{O}_{2-x}$ . The bottom image: The bond length and CN of Ru-O under different applied potentials according to EXAFS fitting results of  $\text{V}_{\text{Mn}}\text{-Ru}_{0.5}\text{Mn}_{0.5}\text{O}_{2-x}$ . Reaction paths and different isotope-labeled  $\text{O}_2$  products of AEM (g) and LOM (h) in the electrolyte using  $\text{H}_2^{16}\text{O}$  as solvent. (i) The ratio of  $^{34}\text{O}_2$ : $^{32}\text{O}_2$  for  $^{18}\text{O}$ -surface labeled  $\text{V}_{\text{Mn}}\text{-Ru}_{0.5}\text{Mn}_{0.5}\text{O}_{2-x}$ ,  $^{18}\text{O}$ -surface labeled  $\text{Ru}_{0.5}\text{Mn}_{0.5}\text{O}_2$ , and  $^{18}\text{O}$ -surface labeled  $\text{C-RuO}_2$  in the electrolyte using  $\text{H}_2^{16}\text{O}$  as the solvent.

To provide an in-depth understanding of the structural evolution of catalyst under acidic OER conditions, we conducted operando XAFS measurements. Before conducting operando XAFS tests, we activated the  $\text{Ru}_{0.5}\text{Mn}_{0.5}\text{O}_2$  electrode under a constant current density to obtain the  $\text{V}_{\text{Mn}}\text{-Ru}_{0.5}\text{Mn}_{0.5}\text{O}_{2-x}$ . The resulting  $\text{V}_{\text{Mn}}\text{-Ru}_{0.5}\text{Mn}_{0.5}\text{O}_{2-x}$  catalyst, which had undergone the self-limiting surface leaching process and contains Mn vacancies, was used for the operando XAFS testing. During the operando XAFS experiment, the voltage applied to  $\text{V}_{\text{Mn}}\text{-Ru}_{0.5}\text{Mn}_{0.5}\text{O}_{2-x}$  was first increased from 1.2 V to 1.6 V vs. RHE, and then reversed back from 1.6 V to 1.2 V vs. RHE (Figure S38). The Ru K-edge XANES spectra recorded at different potentials showed slight changes in absorption energy (Figure 3d and Figure S39). Specifically, the oxidation state of Ru first increased from +3.59 at 1.4 V to +3.78 at 1.6 V and then returned to its

original oxidation state at 1.2 V-back (Figure 3f, top), indicating that neighboring Ru atoms transferred charge to the intermediates involved in the OER. However, the valence state of Mn remained unchanged throughout the OER process, as evidenced by Mn K-edge XANES spectra (Figure S40). These observations indicate that the main active element and site of  $\text{V}_{\text{Mn}}\text{-Ru}_{0.5}\text{Mn}_{0.5}\text{O}_{2-x}$  are Ru and the Ru-O bond. Notably, the valence state of Ru in  $\text{V}_{\text{Mn}}\text{-Ru}_{0.5}\text{Mn}_{0.5}\text{O}_{2-x}$  remained below +4 under OER conditions (Figure 3f, top), preventing overoxidation and dissolution of Ru species. To further examine potential changes in the Ru coordination environment, we conducted Ru K-edge EXAFS fitting analysis for the first-shell coordination (Figure 3e, Figures S41 and S42), with results summarized in Table S8. Changes were observed in the average Ru-O bond length or coordination number (CN) of Ru-O (Figure 3f,



bottom). In addition, after reactions were completed, the coordination number and bond length of Ru-O returned to their original states. Similarly, the Mn-O bond length and coordination number returned to their original state once the applied voltage was removed, as demonstrated by the EXAFS results for Mn K-edge (Figures S43-45 and Table S9). Based on the operando XAS results, a comprehensive analysis of the changes in both oxidation number and local structure during the reaction reveals that Ru, which exhibits alterations in both its oxidation state and local structure, serves as the primary active site. In contrast, Mn, which undergoes changes solely in its local structure without any variation in its oxidation state, functions as the supporting site. It is important to note that the Mn vacancies in the  $V_{\text{Mn}}\text{-Ru}_{0.5}\text{Mn}_{0.5}\text{O}_{2-x}$  effectively stabilize the structure of catalyst, thereby maintaining the stability of oxidation state of Mn during the short-term operando XAFS testing (3.47 h) (Figure S38). Overall,  $V_{\text{Mn}}\text{-Ru}_{0.5}\text{Mn}_{0.5}\text{O}_{2-x}$  catalyst maintained structural stability under OER conditions, confirming its durability for acidic OER applications.

Our study has elucidated the self-limiting surface leaching process of  $\text{Ru}_{0.5}\text{Mn}_{0.5}\text{O}_2$  catalyst by a comprehensive series of characterizations. Next, we examine the OER mechanisms associated with  $\text{Ru}_{0.5}\text{Mn}_{0.5}\text{O}_2$ . Two well-known OER mechanisms include the adsorbate evolution mechanism (AEM) and the lattice oxygen mechanism (LOM). Catalysts that follow the LOM often suffer from stability issues due to the bulk oxygen diffusion and structural reconstruction caused by the continuous formation of oxygen vacancies and dissolution of cations during lattice oxygen redox. To determine which mechanism governs the  $\text{Ru}_{0.5}\text{Mn}_{0.5}\text{O}_2$  catalyst, we conducted operando DEMS measurements via the isotope  $^{18}\text{O}$ -labelling method. We loaded  $V_{\text{Mn}}\text{-Ru}_{0.5}\text{Mn}_{0.5}\text{O}_{2-x}$ , prepared  $\text{Ru}_{0.5}\text{Mn}_{0.5}\text{O}_2$ , and C-RuO<sub>2</sub> onto porous gas-permeable carbon paper electrodes and subjected them to cyclic voltammograms (CV) cycles in the  $\text{H}_2^{18}\text{O}$  electrolyte. If the catalyst operates via the LOM,  $^{18}\text{O}$  would be incorporated into the catalyst surface through lattice oxygen exchange (Figure S46a). Conversely, catalysts following the AEM would not be labeled with  $^{18}\text{O}$  on their surface (Figure S46b). Subsequently, we thoroughly washed the catalysts with abundant  $\text{H}_2^{16}\text{O}$  to remove any surface-adsorbed  $\text{H}_2^{18}\text{O}$ , followed by three CV cycles in an  $\text{H}_2^{16}\text{O}$  electrolyte. During the CV cycle process, we measured the isotope signal of evolved  $\text{O}_2$ . As shown in Figure S47, all three catalysts predominantly released  $^{32}\text{O}_2$ , with a smaller amount of  $^{34}\text{O}_2$ . The  $^{32}\text{O}_2$  signal corresponds to the AEM (Figure 3g), while  $^{34}\text{O}_2$  signal is related to the LOM (Figure 3h). This suggests that the three catalysts primarily follow the AEM rather than the LOM. Notably,  $V_{\text{Mn}}\text{-Ru}_{0.5}\text{Mn}_{0.5}\text{O}_{2-x}$  exhibited the lowest ratio of  $^{34}\text{O}_2$  to  $^{32}\text{O}_2$  (1.16% for  $V_{\text{Mn}}\text{-Ru}_{0.5}\text{Mn}_{0.5}\text{O}_{2-x}$ , 2.43% for  $\text{Ru}_{0.5}\text{Mn}_{0.5}\text{O}_2$ , and 3.87% for C-RuO<sub>2</sub>) (Figure 3i), indicating minimal involvement of the LOM. These findings suggest that Mn doping and cation vacancies play a crucial role in inhibiting lattice oxygen participation, thereby stabilizing the catalyst surface and facilitating high catalyst stability.

In light of the above findings, we have summarized the self-limiting surface leaching mechanism of the  $\text{Ru}_{0.5}\text{Mn}_{0.5}\text{O}_2$

catalyst, as illustrated in Figure 1a. Initially, Mn is uniformly doped into the  $\text{RuO}_2$ , creating a Ru-Mn solid solution oxide with a relatively perfect rutile structure ( $\text{Ru}_{0.5}\text{Mn}_{0.5}\text{O}_2$ ). Subsequently, Mn on the catalyst surface dissolves through the LOM pathway during the initial acidic OER process, resulting in a defective  $\text{Ru}_{0.5}\text{Mn}_{0.5}\text{O}_2$  structure with abundant surface Mn vacancies ( $V_{\text{Mn}}\text{-Ru}_{0.5}\text{Mn}_{0.5}\text{O}_{2-x}$ ). Lastly, the newly formed surface primarily follows the AEM pathway, with the LOM pathway being suppressed, thus inhibiting further leaching of Ru/Mn and achieving stable acidic OER.

### Theoretical calculations

Density functional theory (DFT) calculations were performed to investigate the effects of self-limiting surface leaching on catalytic activity and stability for OER. The fully oxidized (110) surface was chosen to be used in our DFT calculations because the  $\text{RuO}_2(110)$  is the most stable surface in C-RuO<sub>2</sub> catalyst. As shown in Figure 4a and Figure S48, there are two types of Ru site in the terminated layer of  $\text{RuO}_2(110)$  surface: the coordinatively unsaturated site (CUS) with five coordinated O atoms and the fully coordinated bridge site (BRI) with six coordinated O atoms. Our DFT results suggest that, for a Mn dopant, it is energetically favorable to replace the BRI Ru site not the CUS site (Figure 4b). Nevertheless, the experimental results show that the Mn demetallation occurs during OER process, leading to the formation of Mn vacancies. In our simulations, the Mn vacancy at BRI site and the formation of Mn vacancy are shown in Figure 4c and Figure S49, using as the model of  $V_{\text{Mn}}\text{-RuMnO}_{2-x}(110)$  surface. By operando DEMS measurements, we have demonstrated that OER process mainly follows the AEM pathway on the C-RuO<sub>2</sub>,  $\text{RuMnO}_2$ , and  $V_{\text{Mn}}\text{-RuMnO}_{2-x}$ . As depicted schematically in Figure 4d and Figure S50, at the CUS Ru site, the  $4e^-$  OER on  $V_{\text{Mn}}\text{-RuMnO}_{2-x}(110)$  can be triggered from one  $\text{H}_2\text{O}$  molecule adsorption. After two sequential deprotonation steps, it forms the surface-adsorbed O (\*O), which is followed by water nucleophilic attack to form \*OOH intermediate and then the deprotonation of \*OOH to produce  $\text{O}_2$  molecule. Based on the free energy profile of  $\text{RuO}_2(110)$ , the calculated overpotential, as the descriptor of catalytic activity, is about 0.81 V (Figure 4e, Figure S51, and Table S10). It is contributed by the step of \*OOH formation, indicating that the \*OOH formation step is the rate-determining step, consistent with a previous results<sup>44, 45, 58</sup>. Nevertheless, on the  $\text{RuMnO}_2(110)$  surface, the \*OOH intermediate donates a proton to a neighboring oxygen, forming an H-stabilized \*OO species (Figure S52)<sup>48</sup>. This process lowers the free energy barrier for O-O bond formation during the water nucleophilic attack step. As a result, the overpotential of  $\text{RuMnO}_2(110)$  is 0.68 V (Figure 4e and Table S10), meaning that the strategy of Mn doping improves catalytic activity of  $\text{RuO}_2$ . Meanwhile, the H-stabilized \*OO species were also formed on the surface of  $V_{\text{Mn}}\text{-RuMnO}_{2-x}(110)$  (Figure 4d and Figure S50d), promoting the formation of the key \*OOH intermediate. More importantly, the Mn vacancy in  $V_{\text{Mn}}\text{-RuMnO}_{2-x}(110)$  further lowers the free energy barrier of the step of H-stabilized \*OO species formation, thereby regulating the rate-limiting step to obtain the lowest overpotential of 0.50 V among these three different surfaces (Figure 4e and Table S10).



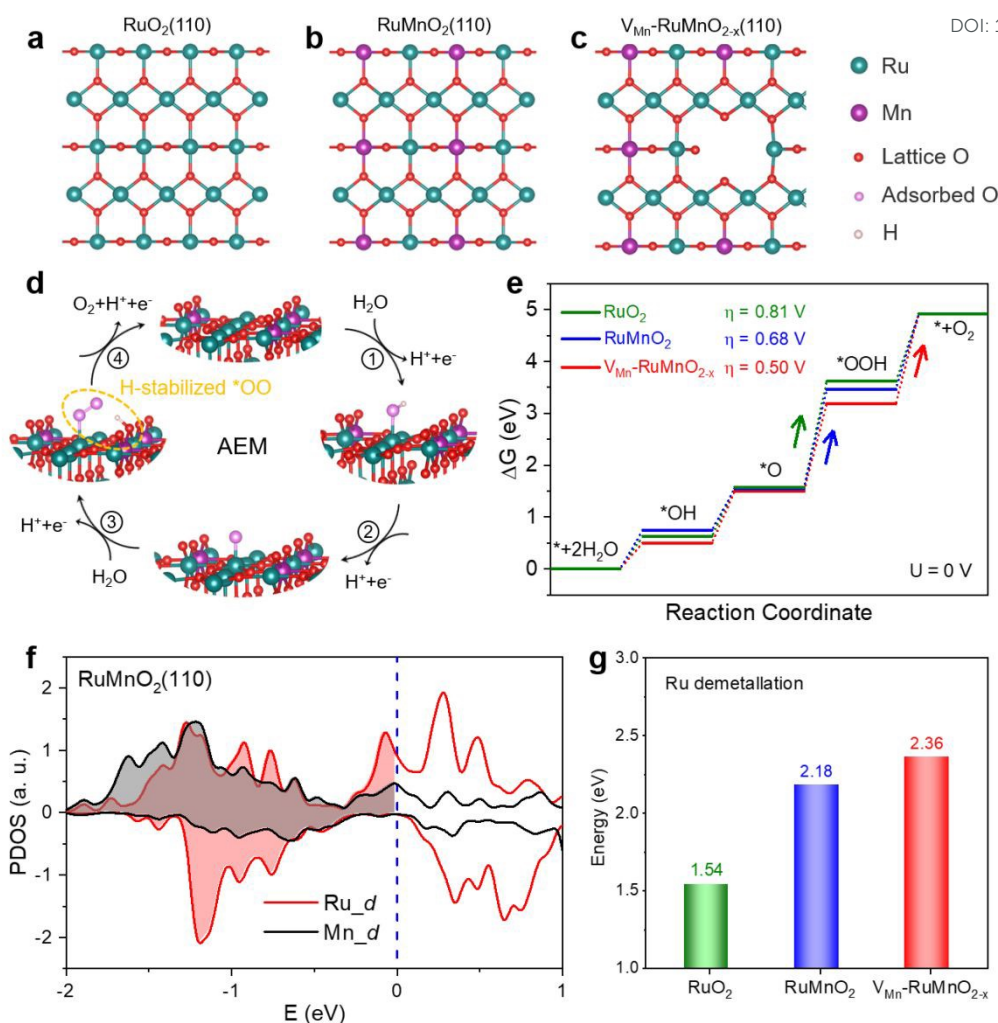


**Figure 4. Theoretical calculations.** Atomistic structures of the surfaces of RuO<sub>2</sub>(110) (a), RuMnO<sub>2</sub>(110) (b), and V<sub>Mn</sub>-RuMnO<sub>2-x</sub>(110) (c). (d) Schematic illustration of AEM for OER on the V<sub>Mn</sub>-RuMnO<sub>2-x</sub>(110) surface. (e) Computed free energy evolution of OER via AEM on surfaces of RuO<sub>2</sub>(110), RuMnO<sub>2</sub>(110) and V<sub>Mn</sub>-RuMnO<sub>2-x</sub>(110) under an electrode potential of 0 V vs. RHE. (f) The projected densities of states (PDOS) of Mn and Ru atom in the top-atom layer of RuMnO<sub>2</sub>(110). (g) Calculated Ru demetallation energies for structural degradation of surfaces of RuO<sub>2</sub>(110), RuMnO<sub>2</sub>(110), and V<sub>Mn</sub>-RuMnO<sub>2-x</sub>(110).

To reveal the formation of Mn vacancies, the PDOS of the Mn and Ru atoms in the top layer of the RuMnO<sub>2</sub>(110) surface are plotted in **Figure 4f**, showing that the density of states below the Fermi level for Mn is lower than that for Ru (such as, ranging from -2 eV to 0 eV). This suggests that the Mn atom is more likely to be oxidized to a higher oxidation state than the Ru atom, which could lead to the easier demetallation of Mn (MnO<sub>4</sub><sup>-</sup>) compared to Ru (RuO<sub>4</sub>), thereby resulting in the formation of Mn vacancies rather than Ru vacancies in Ru<sub>0.5</sub>Mn<sub>0.5</sub>O<sub>2</sub> catalyst. As one of the descriptors of structural stability, the Ru demetallation energy can be calculated based on the proposed mechanism for Ru demetallation (**Figures S53-55**). Compared to the demetallation energy of the RuO<sub>4</sub> for RuO<sub>2</sub>(110) surface (1.54 eV), Mn doping increases the demetallation energy to be 2.18 eV (**Figure 4g**), indicating that Mn doping stabilizes the CUS Ru atom on the RuMnO<sub>2</sub>(110) surface. Importantly, the demetallation energy of RuO<sub>4</sub> further increases to 2.36 eV in V<sub>Mn</sub>-RuMnO<sub>2-x</sub>(110) surface (**Figure 4g**),

suggesting that the formation of Mn vacancies also improve the stability of CUS Ru site. Therefore, these calculations show that the Mn doping and Mn vacancies in V<sub>Mn</sub>-RuMnO<sub>2-x</sub> not only enhance the catalytic activity of Ru sites, but also improve the stability of catalyst.

Actually, the Mn dissolution results in the formation of Mn vacancy (V<sub>Mn</sub>), which changes the coordination of neighboring CUS Ru site, but slightly effect the other CUS Ru atoms that are further away from the V<sub>Mn</sub> site. As a result, the V<sub>Mn</sub> leads to higher density of states below the Fermi level of the CUS Ru atom than that of other Ru atoms further away from the V<sub>Mn</sub> site (such as, ranging from -2 to 0 eV, **Figure S56**). This indicates that the Ru atom neighboring V<sub>Mn</sub> site has a greater ability to resist changes in its valence state compared to other Ru atoms further away from V<sub>Mn</sub> site. In other words, V<sub>Mn</sub> stabilizes the neighboring Ru atoms, but exerts a weaker stabilizing effect on those further from the V<sub>Mn</sub> site. To further support this conclusion, we calculated the demetallation energies of Ru





atoms at various distances from the  $V_{\text{Mn}}$  site. As shown in **Figure S57**, demetallation energies of CUS Ru atoms show a dependency on the distance between the Ru site and the  $V_{\text{Mn}}$  site, and it decreases as the distance increases. Therefore, the  $V_{\text{Mn}}$  tends to inhibit the demetallation of neighboring CUS Ru atom, but slightly effect the Ru atoms that are further away from the  $V_{\text{Mn}}$  site. Meanwhile, the  $V_{\text{Mn}}$  also effects the later Mn dissolution, as confirmed by calculations of the electronic energies of models containing two Mn vacancies at varying distances ( $V_{\text{Mn}}-V_{\text{Mn}}$  distance). As shown in **Figure S58a, b**, the electronic energy depends on  $V_{\text{Mn}}-V_{\text{Mn}}$  distance, increasing as the  $V_{\text{Mn}}-V_{\text{Mn}}$  distance decreases. This indicates that the later  $V_{\text{Mn}}$  formation is more likely to be contributed by the Mn site farther from the  $V_{\text{Mn}}$  site, rather than the Mn site closer to the  $V_{\text{Mn}}$  site. Because the  $V_{\text{Mn}}$  changes the coordination of neighboring Mn atom, but has slight effect on the other Mn atoms further away from this  $V_{\text{Mn}}$  site. It leads to lower density of states of Mn atom close to  $V_{\text{Mn}}$  site compared to those farther away (such as, ranging from -2 eV to 0 eV, **Figure S58c**). This suggests that the Mn atom further away from  $V_{\text{Mn}}$  site is likely to be oxidized to a higher oxidation state, leading to Mn demetallation ( $\text{MnO}_4^-$ ). As a result, these  $V_{\text{Mn}}$  sites tend to be distributed in a scattered manner on the surface.

## Conclusions

In summary, we have clarified the self-limiting surface leaching mechanism in Ru-Mn solid solution oxides, demonstrating its effectiveness in enhancing the long-term stability of catalyst during acidic OER. Specifically, unstable  $\text{RuMnO}_2$  undergoes a transformation into a corrosion-resistant  $V_{\text{Mn}}\text{-RuMnO}_{2-x}$  with abundant surface Mn vacancies through this self-limiting surface leaching process during the initial OER phase. Operando synchrotron characterizations combined with theoretical calculations reveal that cation vacancies and Mn dopants stabilize Ru species by increasing the demetallation energy of Ru active sites, thereby improving the long-term stability of  $V_{\text{Mn}}\text{-RuMnO}_{2-x}$ . Furthermore, the synergy between Mn dopants and cationic vacancies facilitates the formation of H-stabilized \*OO intermediate and regulates the rate-limiting step, effectively lowering the activation free energy and enhancing OER activity. Leveraging these advantages, the  $V_{\text{Mn}}\text{-RuMnO}_{2-x}$  catalyst achieves unprecedented durability alongside exceptional catalytic activity for acidic OER, as verified in practical PEM water electrolyzers. These insights into the self-limiting surface leaching mechanism provide valuable guidance for developing efficient and stable acidic OER catalysts.

## Methods

### Synthesis of $\text{Ru}_{0.5}\text{Mn}_{0.5}\text{O}_2$

Firstly,  $\text{RuCl}_3 \cdot 3\text{H}_2\text{O}$  (0.5 mmol, 130.71 mg) and  $\text{MnCl}_2 \cdot 4\text{H}_2\text{O}$  (0.5 mmol, 98.96 mg) were dissolved in ultra-pure water with vigorous stirring. Ethylenediaminetetraacetic acid disodium salt dihydrate ( $\text{EDTA-2Na}$ ) (0.5 mmol, 186.12 mg) was then added to the mixture, which was stirred for 1 h to form a

homogeneous solution. Subsequently, an excess amount of anhydrous ethanol was added to the solution under stirring, and the precipitated products were collected by centrifugation and washed multiple times with anhydrous ethanol. The obtained sample, referred to as  $\text{Ru}_{0.5}\text{Mn}_{0.5}\text{-EDTA}$  precursors, was heated to 400 °C and held for 2 h at a heating rate of 5 °C  $\text{min}^{-1}$  in a muffle furnace. The resulting black solid powder was washed several times with ultra-pure water to remove NaCl impurities and was denoted as  $\text{Ru}_{0.5}\text{Mn}_{0.5}\text{O}_2$ .

### Synthesis of $\text{Ru}_y\text{Mn}_{1-y}\text{O}_2$ ( $y=0, 0.1, 0.3, 0.7, 0.9, \text{ and } 1$ )

The preparation of the  $\text{Ru}_y\text{Mn}_{1-y}\text{O}_2$  ( $y=0, 0.1, 0.3, 0.7, 0.9, \text{ and } 1$ ) followed the same procedure as for  $\text{Ru}_{0.5}\text{Mn}_{0.5}\text{O}_2$ , except for the adjustment in the amounts of  $\text{RuCl}_3 \cdot 3\text{H}_2\text{O}$  and  $\text{MnCl}_2 \cdot 4\text{H}_2\text{O}$ . Specifically, the total amount of Ru and Mn was kept constant at 0.1 M, with the molar ratio of Ru to Mn set as  $y:(1-y)$ .

### Materials Characterization

Field-emission scanning electron microscopy (FESEM) characterizations were conducted using a SU-8220 instrument. Low-magnification TEM images were obtained on a Hitachi-7650. XRD patterns were recorded using an Ultima IV using  $\text{Cu}_{\text{K}\alpha}$  radiation ( $\lambda=1.5418 \text{ \AA}$ ). ICP-AES was performed on an Optima 7300 DV, and ICP-MS analysis was conducted on a PlasmaQuad 3. XPS data were collected using a Thermo ESCALAB 250Xi with  $\text{Al}_{\text{K}\alpha}$  radiation. Room-temperature EPR spectra of sample were obtained using a JEOL JES-FA200 ESR spectrometer. Soft XAS spectra were acquired at the BL12B-a (MCD) beamline of the NSRL in Hefei, China. HAADF-STEM images and energy-dispersive X-ray spectroscopy (EDX) were captured using a FEI Titan3 G2 60-300 equipped with double spherical aberration correctors. Operando DEMS measurements were conducted with a Hiden HPR-40 DEMS system to record the mass signals of  $^{32}\text{O}_2$  and  $^{34}\text{O}_2$ . X-ray absorption fine structure (XAFS) data were collected at the Wide Energy XAFS beamline (10C beam line) of the Pohang Light Source-II (PLS-II), operated in top-up mode with a ring current of 250 mA at 3.0 GeV.

### Electrochemical Measurement

Electrochemical measurements were carried out using a CHI 760E electrochemical workstation at ambient temperature. Catalyst ink was prepared by dispersing 10 mg of catalyst in 280  $\mu\text{L}$  of ethanol, followed by the addition of 15  $\mu\text{L}$  Nafion solution, and the mixture was stirred vigorously for 2 hours. The OER activity of catalysts was evaluated using a three-electrode configuration, comprising a carbon rod as the counter electrode, an Ag/AgCl (saturated KCl) as the reference electrode, and a glassy carbon electrode (GCE) as the working electrode. For the preparation of the catalyst-coated GCE, 2  $\mu\text{L}$  catalyst ink was dropped onto the GCE (0.19625  $\text{cm}^2$ ), yielding a catalyst loading of 0.35  $\text{mg cm}^{-2}$ . To assess catalytic activity, linear sweep voltammetry (LSV) measurements were performed within the designated potential ranges at a scan rate of 1  $\text{mV s}^{-1}$ , incorporating iR compensation. The Nyquist plots of electrochemical impedance spectroscopy (EIS) were acquired over the frequency range of 10 kHz to 0.1 Hz with an applied





amplitude of 5 mV. Subsequently, OER stability tests were also conducted using a three-electrode system, where the counter electrode was a carbon rod, the reference electrode remained Ag/AgCl (saturated KCl), and carbon paper served as the working electrode. Catalyst-loaded carbon paper electrodes were prepared by applying 40  $\mu\text{L}$  of catalyst ink to carbon paper ( $0.5 \times 1.2 \text{ cm}^2$ ), with a catalyst loading of  $2.26 \text{ mg cm}^{-2}$ . Stability assessments were made through chronopotentiometry tests at constant current density of either  $10 \text{ mA cm}^{-2}$  or  $100 \text{ mA cm}^{-2}$  in a  $0.5 \text{ M H}_2\text{SO}_4$  solution without iR compensation. Additionally, cyclic voltammetry (CV) was performed between 1.2 and 1.5 V vs. RHE at a scan rate of  $100 \text{ mV s}^{-1}$ .

To determine the double-layer capacitance ( $C_{dl}$ ), cyclic voltammetry (CV) measurements were performed within a non-Faradaic potential window of 0.896 to 0.996 V vs. RHE, using scan rates ranging from 10 to  $200 \text{ mV s}^{-1}$ . A linear plot was generated by correlating the current density ( $\Delta j/2$  at 0.946 V vs. RHE) with the scan rate. The slope of this linear fit corresponds to the  $C_{dl}$ . The ECSA was then derived from the  $C_{dl}$  using the following equation:

$$\text{ECSA} = C_{dl} \cdot S / C_s$$

In this equation,  $S$  represents the geometric area of the electrode ( $0.19625 \text{ cm}^2$ ), while  $C_s$  denotes the specific capacitance of the sample. A  $C_s$  constant of  $0.06 \text{ mF cm}^{-2}$  for oxide surfaces in  $\text{H}_2\text{SO}_4$  was applied, as reported in previous reported.

The mass activity values ( $A_{\text{gru}}^{-1}$ ) of the catalysts were calculated by following equation:

$$\text{Mass activity} = \frac{j}{m \times c}$$

where  $j$  represents the current density ( $\text{mA cm}^{-2}$ ) contributed by the Ru active sites at a potential of  $1.45 \text{ V}_{\text{RHE}}$ ,  $m$  represents the catalysts loading on electrode surface ( $\text{mg cm}^{-2}$ ), and  $c$  represents the mass content of Ru in catalysts (%), which was calculated by the ICP-AES results. For  $\text{Ru}_{0.5}\text{Mn}_{0.5}\text{O}_2$ ,  $j = 92.07 \text{ mA cm}^{-2}$ ,  $m = 0.35 \text{ mg cm}^{-2}$ ,  $c = 50.14 \%$ .

In this work, all measured potentials were referenced to the RHE using the equation:  $E_{(\text{RHE})} = E_{(\text{Ag}/\text{AgCl})} + 0.198 \text{ V}$ . The saturated Ag/AgCl reference electrode was calibrated in a high-purity hydrogen-saturated acidic electrolyte ( $0.5 \text{ M H}_2\text{SO}_4$ ), with a platinum wire as the working electrode, a carbon rod as the counter electrode, and the saturated Ag/AgCl as the reference electrode. Cyclic voltammetry (CV) was performed at a scan rate of  $1.0 \text{ mV s}^{-1}$ . The thermodynamic potential for the hydrogen electrode reaction was determined by averaging the two potentials at which the current crossed zero (Figure S59).

### Operando XAFS measurements

Ru and Mn K-edge X-ray absorption fine structure (XAFS) data, including X-ray absorption near edge structure (XANES) and extended X-ray absorption fine structure (EXAFS), were acquired at the Wide Energy XAFS beamline (10C beamline) of the Pohang Light Source-II (PLS-II) in top-up mode, operating at a ring current of 250 mA at 3.0 GeV. The incident beam from the multipole wiggler source was monochromatized using a Si(111) double-crystal monochromator (Bruker ASC). For operando XAFS analysis, a home-made *operando* three-electrode cell with

polyimide film windows was utilized, consisting of a platinum counter electrode, an Ag/AgCl reference electrode, and a working electrode loaded with electrocatalysts on carbon paper (loading area:  $1.5 \text{ cm}^2$ , catalyst loading:  $0.5 \text{ mg cm}^{-2}$ ). Prior to the operando XAFS measurements, the working electrode was activated by running it at a current density of  $50 \text{ mA cm}^{-2}$  in a  $0.5 \text{ M H}_2\text{SO}_4$  electrolyte for 10 h. To obtain more surface information, the incidence angle between the incident beam and the sample were set to below 20 degrees. The operando XAFS measurements were performed during chronoamperometry (CA) experiments at selected potentials in  $0.5 \text{ M H}_2\text{SO}_4$  electrolyte. After stabilization of the current response, XAFS spectra were recorded in fluorescence mode, with a measurement time of about 20 minutes per spectrum. The intensity of the incident X-ray beam was reduced by around 30% to eliminate higher-order harmonic contributions. Energy calibration was conducted simultaneously using reference metal foils for each measurement. The recorded spectra were converted into normalized XANES and Fourier-transformed radial distribution functions (RDFs) using Athena and Artemis software based on standard XAFS procedures. All EXAFS fitting procedures were performed using the Artemis program.

### MEA fabrication and PEM water electrolyzer cell test

The catalyst-coated membrane (CCM) method was employed to construct the membrane electrode assembly (MEA).  $\text{Ru}_{0.5}\text{Mn}_{0.5}\text{O}_2$  or  $\text{Ru}_1\text{Mn}_0\text{O}_2$  served as the anode catalyst, while commercial Pt/C (75 wt%) was utilized as the cathode catalyst, with a Nafion 115 proton exchange membrane acting as the electrolyte. For the preparation of anode and cathode inks, the catalysts were dispersed in a mixture of isopropanol, distilled water, and 5 wt% Nafion<sup>®</sup> solution. After ultrasonication in an ice water bath for at least 30 minutes, a homogeneous catalyst ink was achieved. The anode and cathode catalysts were then air-sprayed directly onto both sides of the Nafion 115 membrane ( $4 \text{ cm}^2$  geometric area) using an ultrasonic spray coating system. Catalyst loadings were controlled at  $4 \text{ mg}_{\text{cat}} \text{ cm}^{-2}$  for the anode and  $0.5 \text{ mg}_{\text{Pt}} \text{ cm}^{-2}$  for the cathode. Finally, the catalyst-coated membranes were hot-pressed at 500 kPa for 3 minutes at  $110 \text{ }^\circ\text{C}$ .

The PEM electrolyzer was constructed with a titanium plate (bipolar plate) at the anode and a graphite plate (bipolar plate) with serpentine flow channels at the cathode. The MEA was sandwiched between a sintered porous titanium plate gas diffusion layer (GDL) on the anode side and a carbon paper GDL on the cathode side. The assembly was tightened to a pressure of 4 N·m. During testing, both the anode and cathode plates were heated to  $60 \text{ }^\circ\text{C}$ , while deionized water preheated to  $60 \text{ }^\circ\text{C}$  was pumped into the anode at a flow rate of  $100 \text{ mL min}^{-1}$ . The performance evaluation of the PEM electrolyzer was carried out using an ITECH IT-M3110 device. Polarization curves of the PEM electrolyzers were recorded over a current density range of 0.01 to  $1.1 \text{ A cm}^{-2}$ . The stability of the electrolyzer was assessed by conducting chronopotentiometry measurements at a constant current density of  $200 \text{ mA cm}^{-2}$ .



### Computational Details

We used Vienna ab initio simulation package (VASP)<sup>59, 60</sup>, with generalized gradient approximation (GGA) in Perdew, Burke, and Ernzerhof (PBE) functional,<sup>61</sup> and projector augmented wave (PAW) method, to perform all density functional theory (DFT) calculations.<sup>62</sup> The plane-waved energy cutoff is set to be 500 eV. The convergence of force between atoms for optimization is set to 0.02 eV/Å, and the convergence of total energy for wave function self-consistent are set to 10<sup>-5</sup> eV. To simulate the surface of RuO<sub>2</sub>, two bottom atom layers are fixed, while the other are fully relaxed. For simulating the surface of RuMnO<sub>2</sub>, all four Mn atoms are located at BRI sites on the top atomic layer, as this configuration results in a lower electronic energy. Since these four doped Mn atoms are equivalent, we created a Mn vacancy by removing one BRI Mn atom and one bonded O atom from the surface model to simulate the surface of V<sub>Mn</sub>-RuMnO<sub>2-x</sub>. The vacuum size is chosen as 18 Å to avoid interaction between two slabs for all structures.

The model we used in DFT calculations can not exactly present the Mn-doping rate, the Mn-doping sites, the proportion of Mn vacancies, as well as the distribution of all V<sub>Mn</sub> sites in the experiment. Nevertheless, our calculations are effective to reveal the effect of V<sub>Mn</sub> on the catalytic activity and stability. This method of DFT investigations have been successfully used to study the doping effect on RuO<sub>2</sub> in other experiments.<sup>2, 48</sup>

### Author contributions

R. G. Cao, J. L. Luo, and S. H. Jiao conceived the experiments and supervised this project. Y. Liu performed the preparation, characterization and performance measurement of the catalyst. X. Y. Li carried out the theoretical calculation. H. Jiang and M. G. Kim performed the XAFS test and analysed the data. J. H. Wu and Y. Deng carried out the HAADF-STEM characterization. X. K. Xi, Z. W. Lei and Y. C. Zhang revised the manuscript. W. S. Yan assisted in conducting the soft XAS experiments. Y. Liu and R. G. Cao wrote the manuscript. All the authors discussed the results and commented on the manuscript.

### Conflicts of interest

There are no conflicts to declare.

### Data availability

The data supporting this article have been included as part of the ESI.†

### Acknowledgements

The authors acknowledge the support from the Strategic Priority Research Program of the Chinese Academy of Sciences (Grant No. XDB0450302), Shenzhen Science and Technology Program (KQTD20190929173914967, ZDSYS20220527171401003), the National Key Research and Development

Program of China (Grant Nos. 2022YFA1504102), the National Natural Science Foundation of China (Grant Nos. 52251105, 22279127, 52072358, U21A2082, 22209162), and the Fundamental Research Funds for the Central Universities (Grant No. YD2060002043). The authors appreciate the support from BL10B and BL12B-a beamlines at the National Synchrotron Radiation Laboratory (NSRL), Hefei, China. This work was partially carried out at the Instruments Center for Physical Science, University of Science and Technology of China (USTC). The authors thank the USTC Supercomputing Center for providing computational resources for this project. The authors also acknowledge the financial support from Gotion High-tech Co., Ltd.

### References

- Z. W. Seh, J. Kibsgaard, C. F. Dickens, I. Chorkendorff, J. K. Nørskov and T. F. Jaramillo, *Science*, 2017, **355**, eaad4998.
- Z.-Y. Wu, F.-Y. Chen, B. Li, S.-W. Yu, Y. Z. Finckro, D. M. Meira, Q.-Q. Yan, P. Zhu, M.-X. Chen, T.-W. Song, Z. Yin, H.-W. Liang, S. Zhang, G. Wang and H. Wang, *Nat. Mater.*, 2022, **22**, 100-108.
- I. Slobodkin, E. Davydova, M. Sananis, A. Breytus and A. Rothschild, *Nat. Mater.*, 2024, **23**, 398-405.
- L. An, C. Wei, M. Lu, H. Liu, Y. Chen, G. G. Scherer, A. C. Fisher, P. Xi, Z. J. Xu and C. H. Yan, *Adv. Mater.*, 2021, **33**, 2006328.
- Z. Shi, J. Li, Y. Wang, S. Liu, J. Zhu, J. Yang, X. Wang, J. Ni, Z. Jiang, L. Zhang, Y. Wang, C. Liu, W. Xing and J. Ge, *Nat. Commun.*, 2023, **14**, 843.
- M. F. Lagadec and A. Grimaud, *Nat. Mater.*, 2020, **19**, 1140-1150.
- J. Kibsgaard and I. Chorkendorff, *Nat. Energy*, 2019, **4**, 430-433.
- Z. Chen, L. Guo, L. Pan, T. Yan, Z. He, Y. Li, C. Shi, Z. F. Huang, X. Zhang and J. J. Zou, *Adv. Energy Mater.*, 2022, **12**, 2103670.
- Q. Shi, C. Zhu, D. Du and Y. Lin, *Chem. Soc. Rev.*, 2019, **48**, 3181-3192.
- F. Liao, K. Yin, Y. Ji, W. Zhu, Z. Fan, Y. Li, J. Zhong, M. Shao, Z. Kang and Q. Shao, *Nat. Commun.*, 2023, **14**, 1248.
- L. Zu, X. Qian, S. Zhao, Q. Liang, Y. E. Chen, M. Liu, B.-J. Su, K.-H. Wu, L. Qu, L. Duan, H. Zhan, J.-Y. Zhang, C. Li, W. Li, J. Y. Juang, J. Zhu, D. Li, A. Yu and D. Zhao, *J. Am. Chem. Soc.*, 2022, **144**, 2208-2217.
- L. C. Seitz, C. F. Dickens, K. Nishio, Y. Hikita, J. Montoya, A. Doyle, C. Kirk, A. Vojvodic, H. Y. Hwang, J. K. Nørskov and T. F. Jaramillo, *Science*, 2016, **353**, 1011-1014.
- S. Hao, H. Sheng, M. Liu, J. Huang, G. Zheng, F. Zhang, X. Liu, Z. Su, J. Hu, Y. Qian, L. Zhou, Y. He, B. Song, L. Lei, X. Zhang and S. Jin, *Nat. Nanotechnol.*, 2021, **16**, 1371-1377.
- Y.-R. Zheng, J. Vernieres, Z. Wang, K. Zhang, D. Hochfilzer, K. Krempel, T.-W. Liao, F. Presel, T. Altantzis, J. Fatermans, S. B. Scott, N. M. Secher, C. Moon, P. Liu, S. Bals, S. Van Aert, A. Cao, M. Anand, J. K. Nørskov, J. Kibsgaard and I. Chorkendorff, *Nat. Energy*, 2021, **7**, 55-64.
- A. Mayyas, M. Ruth, B. Pivovar, G. Bender and K. Wipke, Manufacturing Cost Analysis for Proton Exchange Membrane Electrolyzers <https://www.nrel.gov/docs/fy19osti/72740.pdf> (2019).
- J. Gao, H. Tao and B. Liu, *Adv. Mater.*, 2021, **33**, 2003786.
- J. Ni, Z. Shi, Y. Wang, J. Yang, H. Wu, P. Wang, M. Xiao, C. Liu and W. Xing, *eScience*, 2024, DOI: 10.1016/j.esci.2024.100295.
- L. Hou, X. Gu, X. Cui, J. Tang, Z. Li, X. Liu and J. Cho, *EES Catal.*, 2023, **1**, 619-644.



- 19 K. A. Stoerzinger, R. R. Rao, X. R. Wang, W. T. Hong, C. M. Rouleau and Y. Shao-Horn, *Chem*, 2017, **2**, 668-675.
- 20 C. Roy, R. R. Rao, K. A. Stoerzinger, J. Hwang, J. Rossmeisl, I. Chorkendorff, Y. Shao-Horn and I. E. L. Stephens, *ACS Energy Lett.*, 2018, **3**, 2045-2051.
- 21 C. Rong, K. Dastafkan, Y. Wang and C. Zhao, *Adv. Mater.*, 2023, **35**, 2211884.
- 22 H. Li, Y. Lin, J. Duan, Q. Wen, Y. Liu and T. Zhai, *Chem. Soc. Rev.*, 2024, DOI: 10.1039/d3cs00010a.
- 23 Q. Wang, Y. Cheng, H. B. Tao, Y. Liu, X. Ma, D. S. Li, H. B. Yang and B. Liu, *Angew. Chem. Int. Ed.*, 2023, **62**, e202216645.
- 24 S. Cherevko, A. R. Zeradjanin, A. A. Topalov, N. Kulyk, I. Katsounaros and K. J. J. Mayrhofer, *ChemCatChem*, 2014, **6**, 2219-2223.
- 25 A. Grimaud, O. Diaz-Morales, B. Han, W. T. Hong, Y.-L. Lee, L. Giordano, K. A. Stoerzinger, M. T. M. Koper and Y. Shao-Horn, *Nat. Chem.*, 2017, **9**, 457-465.
- 26 K. Klyukin, A. Zagalskaya and V. Alexandrov, *J. Phys. Chem. C*, 2019, **123**, 22151-22157.
- 27 A. Li, H. Ooka, N. Bonnet, T. Hayashi, Y. Sun, Q. Jiang, C. Li, H. Han and R. Nakamura, *Angew. Chem.*, 2019, **131**, 5108-5112.
- 28 F.-Y. Chen, Z.-Y. Wu, Z. Adler and H. Wang, *Joule*, 2021, **5**, 1704-1731.
- 29 W. Zhao, Y. Liu, X. Fu and W. Wang, *Renewables*, 2023, **1**, 638-667.
- 30 Z. Wang, X. Guo, J. Montoya and J. K. Nørskov, *npj Comput. Mater.*, 2020, **6**, 160.
- 31 L. Chong, G. Gao, J. Wen, H. Li, H. Xu, Z. Green, J. D. Sugar, A. J. Kropf, W. Xu, X. M. Lin, H. Xu, L. W. Wang and D. J. Liu, *Science*, 2023, **380**, 609-616.
- 32 S. Cherevko, S. Geiger, O. Kasian, N. Kulyk, J.-P. Grote, A. Savan, B. R. Shrestha, S. Merzlikin, B. Breitbach, A. Ludwig and K. J. J. Mayrhofer, *Catal. Today*, 2016, **262**, 170-180.
- 33 M. Guo, R. Deng, C. Wang and Q. Zhang, *J. Energy Chem.*, 2023, **78**, 537-553.
- 34 G. Zhao, W. Guo, M. Shan, Y. Fang, G. Wang, M. Gao, Y. Liu, H. Pan and W. Sun, *Adv. Mater.*, 2024, **36**, e2404213.
- 35 W. Liu, Z. Duan and W. Wang, *J. Phys. Chem. C*, 2023, **127**, 5334-5342.
- 36 J. Chen, Y. Ma, T. Huang, T. Jiang, S. Park, J. Xu, X. Wang, Q. Peng, S. Liu, G. Wang and W. Chen, *Adv. Mater.*, 2024, **36**, 2312369.
- 37 L. An, F. Yang, C. Fu, X. Cai, S. Shen, G. Xia, J. Li, Y. Du, L. Luo and J. Zhang, *Adv. Funct. Mater.*, 2022, **32**, 2200131.
- 38 C. F. Dickens and J. K. Nørskov, *J. Phys. Chem. C*, 2017, **121**, 18516-18524.
- 39 D. Galyamin, J. Torrero, I. Rodríguez, M. J. Kolb, P. Ferrer, L. Pascual, M. A. Salam, D. Gianolio, V. Celorrio, M. Mokhtar, D. Garcia Sanchez, A. S. Gago, K. A. Friedrich, M. A. Peña, J. A. Alonso, F. Calle-Vallejo, M. Retuerto and S. Rojas, *Nat. Commun.*, 2023, **14**, 2010.
- 40 Y. Qin, T. Yu, S. Deng, X.-Y. Zhou, D. Lin, Q. Zhang, Z. Jin, D. Zhang, Y.-B. He, H.-J. Qiu, L. He, F. Kang, K. Li and T.-Y. Zhang, *Nat. Commun.*, 2022, **13**, 3784.
- 41 X. Bai, X. Zhang, Y. Sun, M. Huang, J. Fan, S. Xu and H. Li, *Angew. Chem. Int. Ed.*, 2023, **62**, e202308704.
- 42 C. Lin, J.-L. Li, X. Li, S. Yang, W. Luo, Y. Zhang, S.-H. Kim, D.-H. Kim, S. S. Shinde, Y.-F. Li, Z.-P. Liu, Z. Jiang and J.-H. Lee, *Nat. Catal.*, 2021, **4**, 1012-1023.
- 43 S. Hao, M. Liu, J. Pan, X. Liu, X. Tan, N. Xu, Y. He, L. Lei and X. Zhang, *Nat. Commun.*, 2020, **11**, 5368.
- 44 D. Zhang, M. Li, X. Yong, H. Song, G. I. N. Waterhouse, Y. Yi, B. Xue, D. Zhang, B. Liu and S. Lu, *Nat. Commun.*, 2023, **14**, 2517.
- 45 Y. Shen, X.-L. Zhang, M.-R. Qu, J. Ma, S. Zhu, Y.-L. Min, M.-R. Gao and S.-H. Yu, *Nat. Commun.*, 2024, **15**, 7861. DOI: 10.1039/D4EE05220J
- 46 Y. Li, W. Wang, M. Cheng, Y. Feng, X. Han, Q. Qian, Y. Zhu and G. Zhang, *Adv. Mater.*, 2023, **35**, 2206351.
- 47 L. Hou, Z. Li, H. Jang, Y. wang, X. Cui, X. Gu, M. G. Kim, L. Feng, S. Liu and X. Liu, *Adv. Energy Mater.*, 2023, **13**, 2300177.
- 48 H. Jin, X. Liu, P. An, C. Tang, H. Yu, Q. Zhang, H.-J. Peng, L. Gu, Y. Zheng, T. Song, K. Davey, U. Paik, J. Dong and S.-Z. Qiao, *Nat. Commun.*, 2023, **14**, 354.
- 49 J. Zhu, Y. Guo, F. Liu, H. Xu, L. Gong, W. Shi, D. Chen, P. Wang, Y. Yang, C. Zhang, J. Wu, J. Luo and S. Mu, *Angew. Chem. Int. Ed.*, 2021, **60**, 12328-12334.
- 50 N. Yao, H. Jia, J. Zhu, Z. Shi, H. Cong, J. Ge and W. Luo, *Chem*, 2023, **9**, 1882-1896.
- 51 J. Wang, C. Cheng, Q. Yuan, H. Yang, F. Meng, Q. Zhang, L. Gu, J. Cao, L. Li, S.-C. Haw, Q. Shao, L. Zhang, T. Cheng, F. Jiao and X. Huang, *Chem*, 2022, **8**, 1673-1687.
- 52 Y. Yao, S. Hu, W. Chen, Z.-Q. Huang, W. Wei, T. Yao, R. Liu, K. Zang, X. Wang, G. Wu, W. Yuan, T. Yuan, B. Zhu, W. Liu, Z. Li, D. He, Z. Xue, Y. Wang, X. Zheng, J. Dong, C.-R. Chang, Y. Chen, X. Hong, J. Luo, S. Wei, W.-X. Li, P. Strasser, Y. Wu and Y. Li, *Nat. Catal.*, 2019, **2**, 304-313.
- 53 C. Rong, X. Shen, Y. Wang, L. Thomsen, T. Zhao, Y. Li, X. Lu, R. Amal and C. Zhao, *Adv. Mater.*, 2022, **34**, 2110103.
- 54 Y. Wen, C. Liu, R. Huang, H. Zhang, X. Li, F. P. García de Arquer, Z. Liu, Y. Li and B. Zhang, *Nat. Commun.*, 2022, **13**, 4871.
- 55 J. Liu, T. Wang, Z. Lin, M. Liao, S. Liu, S. Wang, Z. Cai, H. Sun, Y. Shen, Y. Huang and Q. Li, *Energy Environ. Sci.*, 2024, **17**, 3088-3098.
- 56 K. Wang, Y. Wang, B. Yang, Z. Li, X. Qin, Q. Zhang, L. Lei, M. Qiu, G. Wu and Y. Hou, *Energy Environ. Sci.*, 2022, **15**, 2356-2365.
- 57 Z. L. Zhao, Q. Wang, X. Huang, Q. Feng, S. Gu, Z. Zhang, H. Xu, L. Zeng, M. Gu and H. Li, *Energy Environ. Sci.*, 2020, **13**, 5143-5151.
- 58 Y. Wang, X. Lei, B. Zhang, B. Bai, P. Das, T. Azam, J. Xiao and Z. S. Wu, *Angew. Chem. Int. Ed.*, 2023, **63**, e202316903.
- 59 G. Kresse and J. Hafner, *Physical Review B*, 1993, **47**, 558-561.
- 60 G. Kresse and J. Hafner, *Phys. Rev. B Condens Matter*, 1994, **49**, 14251-14269.
- 61 J. P. Perdew, K. Burke and M. Ernzerhof, *Phys. Rev. Lett.*, 1996, **77**, 3865-3868.
- 62 P. E. Blöchl, *Phys. Rev. B Condens Matter*, 1994, **50**, 17953-17979.



## Data Availability Statement

The data supporting this article have been included as part of the Supplementary Information.

